Spatial Decorrelation in GNSS-Based SAR Coherent Change Detection

Qilei Zhang, Michail Antoniou, Wenge Chang, and Mikhail Cherniakov

Abstract—**This paper analyzes the spatial decorrelation between repeat-pass bistatic synthetic aperture radar (BSAR) images with Global Navigation Satellite Systems as transmitters and a fixed receiver. This study is needed in the development of such a system to monitor temporal changes in a scene. The main challenge is that, in this bistatic configuration, spatial coherence heavily depends on the data acquisition geometry. The appropriate theoretical framework to describe spatial coherence for this case is developed by extending well-established monostatic models and, in principle, can be applied to any fixed-receiver BSAR with a spaceborne transmitter. Theoretical results are initially supported by Monte Carlo simulations. Finally, the validity of the model is confirmed by comparing real images.**

Index Terms—**Bistatic synthetic aperture radar (BSAR), coherent change detection (CCD), GNSS-based SAR, spatial decorrelation.**

I. INTRODUCTION

OVER the last few years, the feasibility of bistatic synthetic aperture radar (BSAR) has been established. A number of different topologies have been investigated, and their imaging capability has been experimentally demonstrated [1]–[5]. Research is now moving toward the exploitation of BSAR imagery for Earth observation and monitoring [6]–[9].

One such BSAR configuration is Global Navigation Satellite Systems (GNSS) based SAR. This technology comprises navigation satellites (such as GPS, GLONASS, Galileo, and Compass) as transmitters of opportunity, while the receiver could be moving (airborne/on ground moving vehicle etc.) or fixed on the ground [10]. In this paper, a fixed-receiver configuration is assumed. Potentially, Galileo satellites are to be used due to their much higher resolution performance (about 8 m × 5 m in range and azimuth, respectively) compared to those provided by other navigation satellites. However, until Galileo is fully operational, GLONASS is being used with a resolution of 30 m × 5 m. The reader is prompted to [11]–[14] for previous work with a moving receiver setup.

Q. Zhang and W. Chang are with the College of Electronic Science and Engineering, National University of Defense Technology, Changsha, Hunan 410073, China (e-mail: zhangqilei1985@gmail.com; changwenge@nudt.edu.cn).

M. Antoniou and M. Cherniakov are with the School of Electronic, Electrical and Computer Engineering, University of Birmingham, B15 2TT Birmingham, U.K. (e-mail: m.antoniou@bham.ac.uk).

The proposed application for such a system is surface displacement monitoring in local areas. Some examples include the following:

1) temporal change detection due to earthwork movement in large engineering structures (e.g., highway earthworks, bridges, and dams) or new infrastructure projects during their construction stage;
2) slope stability monitoring, e.g., in open pit mines;
3) situational awareness in infrastructure networks (highway/railway), particularly during adverse weather conditions, to warn of incipient or actual faults (e.g., landslips in extreme rain or fallen trees in extreme wind conditions).

Taking into account the permanent GNSS coverage of any point on Earth, a fixed receiver overlooking an area of interest, typically a few square kilometers wide, may potentially provide persistent monitoring, which is one of the requirements for the aforementioned applications. In addition, the multitude of satellites viewing the same area from different angles (six to eight satellites for a given GNSS) provides the option to choose the best bistatic configuration in terms of resolution and shadow reduction. Moreover, such applications do not require fine resolutions or large stand-off distances between the sensor and the observation area (typically, they do not exceed 200 m), so the coarse resolution and limited operational range of the proposed technology do not pose any major limitations. Furthermore, GNSS operate in the L-band, which makes them attractive for Earth observation. Finally, the architecture of the receiving segment is no different to that of a conventional navigation receiver, which makes this technology more cost-effective.

As the first stage in this research, a coherent change detector (CCD) is being built to detect temporal scene changes. Different aspects of this technology have been considered on the theoretical and practical levels in [15]–[18]. This technique compares consecutive images of the same scene, temporally separated by the revisit cycle of a single satellite, at the phase level. Assuming that the interrogated surface has changed between satellite passes, image pairs will be decorrelated, and this decorrelation can be used to quantify the level of surface deformation. A complete treatise of CCD for monostatic SAR can be found in [19], where the theoretical and experimental work for detecting fine-scale scene changes using repeat-pass SAR images has been investigated both on the signal processing and physical levels.

The next problem to tackle in this development is that image decorrelation contains not only factors associated with temporal scene displacements (temporal decorrelation) but also other
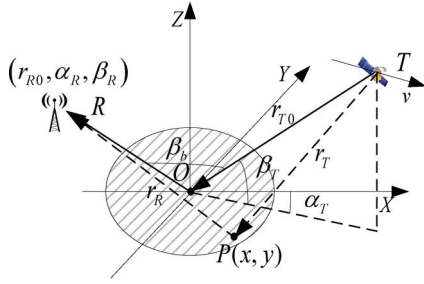
Fig. 1.   GNSS-based SAR geometry.

decorrelation factors that may corrupt it [20]. One of the main decorrelation sources is spatial (or geometric) decorrelation [21], which arises from the fact that it is difficult, if possible at all, to have identical satellite trajectories in repeat passes. Changes in the observation geometry between passes lead to different relative positions between the radar and the scattering centers within a resolution cell, and this results in changes to the phase of the backscattered signals.

Analysis of the spatial decorrelation for monostatic SAR has been well presented in the literature [22]–[26]. However, this effect is essentially different for BSAR due to the different geometries involved and even more for GNSS-based SAR with its essentially asymmetric topology and the peculiarities of its ambiguity function [17]. The main challenge is that, in bistatic configurations, spatial coherence depends on the data acquisition geometry directly. This means that some acquisitions are more robust to it, while in some others, a complete loss of image coherence may occur, rendering any CCD impossible. For this reason, this problem was studied both at the theoretical and practical levels.

The aim of this paper is to present a spatial decorrelation analysis for GNSS-based SAR. The theoretical model of spatial decorrelation is developed based on the 'speckle' model [27] and the generalized ambiguity function [28] in Section II. Spatial decorrelation effects for three different GNSS-based SAR configurations are calculated in Section III. Theoretical results are confirmed by Monte Carlo simulation in Section IV, followed by confirmation using experimental data in Section V.

II. THEORETICAL MODEL

Considering two complex SAR image pixels s_1 and s_2, the correlation coefficient between them can be evaluated as [21]

$$\rho = \frac{|\langle s_1 s_2^* \rangle|}{\sqrt{\langle s_1 s_1^* \rangle \langle s_2 s_2^* \rangle}} \tag{1}$$

where $\langle \cdot \rangle$ denotes ensemble averaging. From (1), it can be seen that $0 \leq \rho \leq 1$, and the only condition for $\rho = 1$ is $s_1 = s_2$. In practice, s_1 and s_2 consist of uncorrelated components due to different decorrelation sources. In SAR interferometric or CCD applications, there are three major decorrelation factors, namely, thermal noise and temporal and spatial decorrelations [20]. This paper only considers the latter factor.

Spatial decorrelation is due to the slightly different viewing angles between two repeat-pass data acquisition geometries. Fig. 1 shows the imaging geometry of GNSS-based SAR to be

used in this analysis. The point O is the center of a resolution cell in the imaging scene. It is convenient to establish the coordinate system in such a way that O is at the coordinate origin and the XOY plane coincides with the ground plane. The synthetic aperture center of the satellite trajectory is at point T, and the velocity of the satellite is v. The position of the satellite at point T is determined by $(r_{T0}, \alpha_T, \beta_T)$, where r_{T0} is the distance from O to T and α_T and β_T are the azimuth and elevation angles of the satellite, respectively. The position of the fixed receiver R can be determined by the corresponding parameters $(r_{R0}, \alpha_R, \beta_R)$.

As shown in Fig. 1, $P(x, y)$ is a point in the vicinity of O, i.e., it is a point scatterer within the resolution cell. The distance between $P(x, y)$ and T can be expressed as

$$r_T(x, y, r_{T0}, \alpha_T, \beta_T) \approx r_{T0} - x \cos \alpha_T \cos \beta_T$$
$$+ y \sin \alpha_T \cos \beta_T. \tag{2}$$

According to the "speckle" model [21], [27], the complex image pixel s without the system thermal noise, measured at position O, may be represented as the sum of complex returns of all of the point scatterers within the resolution cell

$$s = \iint \sigma(x, y) \exp \left[-j \frac{2\pi}{\lambda} \left(r_T(x, y, r_{T0}, \alpha_T, \beta_T) \right. \right.$$
$$\left. \left. + r_R(x, y, r_{R0}, \alpha_R, \beta_R) \right) \right] \cdot W(x, y) \, dx \, dy. \tag{3}$$

Equation (3) represents the image pixel after image formation processing, where $\sigma(x, y)$ represents the complex backscatter coefficient at each point on the plane, r_R is the distance from target $P(x, y)$ to the receiver, λ is the radar wavelength, and $W(x, y)$ is the point spread function (PSF).

According to [28], the PSF of GNSS-based SAR with a linear satellite trajectory can be given as

$$|W(x, y)| \approx \text{tri} \left(\frac{2 \cos \left(\frac{\beta_b}{2} \right) \mathbf{\Theta}^T \mathbf{P}(x, y)}{c \cdot \delta_\tau} \right)$$
$$\cdot \text{sinc} \left(\frac{2 \omega_E \mathbf{\Xi}^T \mathbf{P}(x, y)}{\lambda \cdot \delta_d} \right) \tag{4}$$

where $\text{tri}(\cdot)$ is the triangular function, specifying that the range resolutions for transmitted signals of GNSS are pseudorandom sequences, and $\text{sinc}(\cdot)$ specifies azimuth resolution. The parameter β_b is the bistatic angle (as shown in Fig. 1, the angle between vectors $\overrightarrow{TO}$ and $\overrightarrow{RO}$), $\mathbf{\Theta}$ is the unit vector in the direction along the bisector of β_b, ω_E is the equivalent bistatic angular speed, $\mathbf{\Xi}$ is a unit vector along the satellite's motion direction, and $\mathbf{P}(x, y)$ is the position vector of a scattering point P relevant to the origin. The parameter $\mathbf{\Theta}$ is generally defined as the direction of range resolution and $\mathbf{\Xi}$ as that of azimuth resolution [28]. In (4), $\delta_\tau = 1/B$ and $\delta_d = 1/T_{\text{sys}}$ are the time delay and Doppler resolutions, respectively, where B is the bandwidth of the transmitted signal and T_{sys} is the dwell time on target.

On the basis that a fixed-receiver configuration is used, the only differences between repeat-pass data acquisition geometries are due to the trajectory of the satellite in each pass. This

implies that the primary and repeat SAR images of the same ground patch can be expressed as

$$
s_1 = \iint \sigma(x,y) \exp\left[-j\frac{2\pi}{\lambda}\left(r_T(x,y,r_{T0},\alpha_{T1},\beta_{T1})\right.\right.
$$
$$
\left.\left. + r_R(x,y,r_{R0},\alpha_R,\beta_R))\right]\right.
$$
$$
\cdot W(x,y)\,dx\,dy \tag{5}
$$
$$
s_2 = \iint \sigma(x,y) \exp\left[-j\frac{2\pi}{\lambda}\left(r_T(x,y,r'_{T0},\alpha_{T2},\beta_{T2})\right.\right.
$$
$$
\left.\left. + r_R(x,y,r_{R0},\alpha_R,\beta_R))\right]\right.
$$
$$
\cdot W(x,y)\,dx\,dy. \tag{6}
$$

Moreover, we assume that the coregistration of the primary and repeat SAR images has been performed. Therefore, the cross-correlation of the two signals is

$$
s_1 s_2^* = \iint \iint \sigma(x,y)\sigma^*(x',y')
$$
$$
\times \exp\left[-j\frac{2\pi}{\lambda}\left(r_T(x,y,r_{T0},\alpha_{T1},\beta_{T1})\right.\right.
$$
$$
\left.\left. + r_R(x,y,r_{R0},\alpha_R,\beta_R))\right] W(x,y)\right.
$$
$$
\times \exp\left[j\frac{2\pi}{\lambda}\left(r_T(x',y',r'_{T0},\alpha_{T2},\beta_{T2})\right.\right.
$$
$$
\left.\left. + r_R(x',y',r_{R0},\alpha_R,\beta_R))\right]\right.
$$
$$
\times W^*(x',y')\,dx\,dy\,dx'\,dy'. \tag{7}
$$

Assuming that the imaged surface consists of uniformly distributed and uncorrelated scattering centers [21]

$$
\langle \sigma(x,y)\sigma^*(x',y')\rangle = \sigma_0^2 \cdot \delta(x-x',y-y') \tag{8}
$$

where σ_0 is the average complex backscatter coefficient, then (7) can be reduced to

$$
\langle s_1 s_2^*\rangle = \sigma_0^2 \cdot \iint \exp\left[-j\frac{2\pi}{\lambda}\left(r_T(x,y,r_{T0},\alpha_{T1},\beta_{T1})\right.\right.
$$
$$
\left.\left. - r_T(x,y,r'_{T0},\alpha_{T2},\beta_{T2}))\right]\right.
$$
$$
\times |W(x,y)|^2 \, dx\,dy
$$
$$
= \sigma_0^2 \cdot \exp\left(-j\frac{2\pi}{\lambda}(r_{T0}-r'_{T0})\right)
$$
$$
\cdot \iint \exp\left[-j\frac{2\pi}{\lambda}(x \cdot U + y \cdot V)\right]
$$
$$
\times |W(x,y)|^2 \, dx\,dy \tag{9}
$$

where U and V are determined by the position offset of the transmitter

$$
U = \cos\alpha_{T2}\cos\beta_{T2} - \cos\alpha_{T1}\cos\beta_{T1} \tag{10}
$$
$$
V = \sin\alpha_{T1}\cos\beta_{T1} - \sin\alpha_{T2}\cos\beta_{T2}. \tag{11}
$$

Similarly, the autocorrelation of image pixels can be given as

$$
\langle s_1 s_1^*\rangle = \langle s_2 s_2^*\rangle = \sigma_0^2 \cdot \iint |W(x,y)|^2 \, dx\,dy. \tag{12}
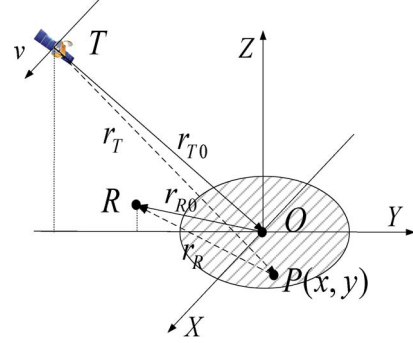$$

Fig. 2. Quasi-monostatic configuration.

Substituting (9) and (12) in (1) and simplifying, the correlation coefficient caused by spatial decorrelation can be calculated by

$$
\rho = \frac{\left|\iint \exp\left[-j\frac{2\pi}{\lambda}(x \cdot U + y \cdot V)\right] |W(x,y)|^2 \, dx\,dy\right|}{\iint |W(x,y)|^2 \, dx\,dy}. \tag{13}
$$

From (13), the spatial coherence is equal to 1 if $U = V = 0$. In all other cases, $0 \le \rho < 1$. In addition, the calculation of (13) is also dependent on the PSF $W(x,y)$.

III. SPATIAL DECORRELATION FOR DIFFERENT BISTATIC TOPOLOGIES

In this section, the spatial decorrelation for GNSS-based SAR will be evaluated for different satellite geometries. The first one is the quasi-monostatic configuration, where the satellite flies directly behind the receiver. This configuration is chosen as it bears the closest resemblance to a monostatic system. The second case is the nadir-looking configuration, where the satellite flies above the receiver. This is a more practical scenario from an operational point of view since a low-gain antenna can simply be pointed upward to record the direct satellite signal for synchronization purposes. The final case is the general bistatic case.

In the first two cases, it is possible to obtain a closed (or quasi-closed) form solution for (13). In the general case, (13) does not have an analytical solution, and therefore, spatial decorrelation is evaluated numerically.

A. Quasi-Monostatic Configuration

As shown in Fig. 2, let us consider a particular configuration named as the quasi-monostatic configuration, where $\alpha_T = \alpha_R = \pi/2$, and the satellite is assumed to move parallel to the X-axis. In this case, the direction of ground range resolution R_r is along the Y-axis, and the direction of ground azimuth resolution R_a is along the X-axis. According to (4), we will have

$$
W(x,y) = \text{tri}\left(\frac{y}{R_r}\right) \cdot \text{sinc}\left(\frac{x}{R_a}\right) \tag{14}
$$

where

$$
\begin{cases} R_r = \frac{c\delta_\tau}{2\cos^2(\beta_b/2)} \\ R_a = \frac{\delta_d \lambda}{2\omega_E}. \end{cases} \tag{15}
$$

The PSF can be divided into the responses along the X- and Y-axes. Therefore, the double integral shown in (13) can be replaced by the multiplication of two one-variable integrals. Then, according to the definition of Fourier transform, we can get

$$\rho = \left(1 - \left|\frac{U}{\lambda} \cdot R_a\right|\right) \cdot \mathbf{F}\left(\text{tri}^2\left(\frac{y}{R_r}\right), V\right) \quad (16)$$

where

$$\mathbf{F}\left(\text{tri}\left(\frac{y}{R_r}\right), V\right)$$
$$= \frac{3}{2} \cdot \int \exp\left[-j\frac{2\pi}{\lambda} y \cdot R_r \cdot V\right] \text{tri}^2(y)\, dy. \quad (17)$$

From (16), we can conclude that the spatial decorrelation effect of quasi-monostatic configuration consists of components along both azimuth and range resolution directions. This is quite different from the result of monostatic configuration, where only the spatial decorrelation effect along the range resolution direction is usually considered [21]. In the next sections, the spatial decorrelation is evaluated for offsets in the azimuth and elevation angles of the satellite separately.

Azimuth Offsets: If the elevation angle is assumed to be fixed, i.e., $\beta_{T1} = \beta_{T2} = \beta$ and only the azimuth angle offset $\delta\alpha = \alpha_{T1} - \alpha_{T2}$ is considered, (16) reduces to

$$\begin{cases} U = \cos\beta \cdot (\cos\alpha_{T2} - \cos\alpha_{T1}) = \cos\beta\sin\alpha\delta\alpha \\ V = \cos\beta \cdot (\sin\alpha_{T1} - \sin\alpha_{T2}) = \cos\beta\cos\alpha\delta\alpha \end{cases} \quad (18)$$

where $\alpha = (\alpha_{T1} + \alpha_{T2})/2$. For the quasi-monostatic configuration and assuming that the offset is slight, then $\alpha \approx \pi/2$. Hence, $U \approx \cos\beta \cdot \delta\alpha$, $V \approx 0$. In this case, $\mathbf{F}(\text{tri}(y/R_r), V) \approx 1$, and (16) becomes

$$\rho = 1 - \frac{|\cos\beta\delta\alpha|}{\lambda} \cdot R_a. \quad (19)$$

Elevation Offsets: Similarly, if the azimuth angle is assumed to be fixed, i.e., $\alpha_{T1} = \alpha_{T2} = \pi/2$ and only the elevation angle offset $\delta\beta = \beta_{T1} - \beta_{T2}$ is considered, then

$$\begin{cases} U = 0 \\ V \approx \sin\beta \cdot \delta\beta \end{cases} \quad (20)$$

where $\beta = (\beta_{T1} + \beta_{T2})/2$. Thus

$$\rho = \mathbf{F}\left(\text{tri}^2\left(\frac{y}{R_r}\right), \sin\beta \cdot \delta\beta\right). \quad (21)$$

The spatial decorrelation coefficient due to different azimuth (19) or elevation (21) offsets is plotted in Fig. 3 for an example quasi-monostatic configuration. The calculation parameters correspond to those of a GLONASS satellite and are listed in Table I. It is assumed that the satellite azimuth and elevation angles in the first pass are $\alpha_{T1} = 90°$ and $\beta_{T1} = 60°$. The 2-D resolution can be calculated using (15) for the listed parameters as $R_a = 3.04$ m and $R_r = 39.14$ m.

It can be seen from Fig. 3 that the correlation coefficient decreases as the angular offset increases, as expected. Moreover, the spatial decorrelation due to elevation offsets is much
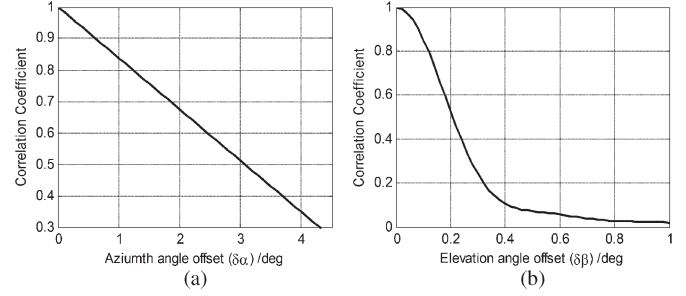

Fig. 3. Spatial decorrelation in quasi-monostatic configuration due to (a) azimuth and (b) elevation angle offsets.

TABLE I
CALCULATION PARAMETERS

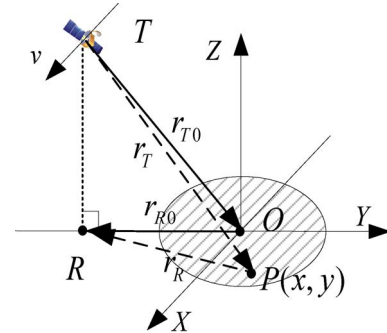| Parameters	Value
Satellite effective velocity	3953 m/s
Carrier Frequency	1602.5625 MHz
Signal Bandwidth	5.11 MHz
Integration Time	300 s
Satellite-to-Target Range r_{T0}	19284 Km
Receiver Azimuth Angle	90 deg
Receiver Elevation Angle	5 deg

Fig. 4. Nadir-looking configuration.

more sensitive than those due to azimuth offsets. The main reason for this is the difference in the range and azimuth resolutions. Inspection of (19) and (21) demonstrates that spatial decorrelation due to azimuth offsets depends on azimuth resolution, whereas that due to elevation offsets depends on range resolution. Since $R_r \gg R_a$ for GNSS-based SAR, the sensitivity to spatial effects is more pronounced in (21).

B. Nadir-Looking Configuration

As shown in Fig. 4, in the nadir-looking configuration, the receiver is at the nadir point of the satellite, and it is assumed that $\alpha_T = \alpha_R = \pi/2$.

Since the distance from the transmitter to the target is far longer than that from the receiver to the target, the elevation angle and the bistatic angle satisfy $\beta_b \approx \beta_T = \pi/2$. Assuming that the satellite's motion is parallel to the X-axis as well, the
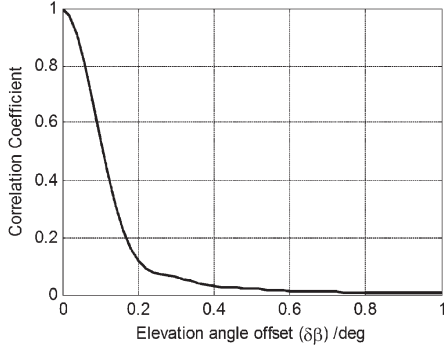
Fig. 5. Spatial decorrelation effect in nadir-looking configuration.
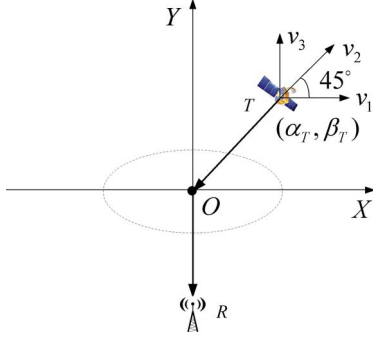

Fig. 6. Top view of the general bistatic configuration.

system impulse response can be expressed as in (14), and (16) still holds, rewritten here for convenience

$$\rho = \left(1 - \left| \frac{U}{\lambda} \cdot R_a \right| \right) \cdot \mathbf{F} \left(\text{tri}^2 \left(\frac{y}{R_r} \right), V \right). \quad (22)$$

However, in this case, the ground range resolution (15) changes to $R_r = c\delta_\tau$.

If only the azimuth angle offset is considered, i.e., $\beta_{T1} = \beta_{T2} = \pi/2$, then $U = 0$, $V = 0$, and the correlation coefficient is equal to 1. This means that, in the nadir-looking configuration, there is no spatial decorrelation due to azimuthal offsets. In terms of offsets in the elevation angle, assuming that $\alpha_{T1} = \alpha_{T2} = \pi/2$, then $U = 0$, and $V \approx \sin\beta\delta\beta$. According to the definition of nadir-looking geometry, we get $\beta = \pi/2$, and then, $V \approx \delta\beta$. Therefore, the spatial decorrelation can be given as

$$\rho = \mathbf{F} \left(\text{tri}^2 \left(\frac{y}{R_r} \right), \delta\beta \right). \quad (23)$$

The spatial decorrelation versus the offset in satellite elevation angles is shown in Fig. 5 for the example of Table I. It can be seen that the correlation coefficient decreases sharply with the offset in elevation angle. For an error of $0.2°$, the correlation coefficient is approximately 0.1, whereas for the quasi-monostatic case, it is equal to 0.5.

C. General Bistatic Configuration

In the general bistatic configuration, the PSF (4) cannot be reduced to a simpler function as in (14) and also does not have a closed-form solution. Therefore, spatial decorrelation in the general case (13) is evaluated numerically.
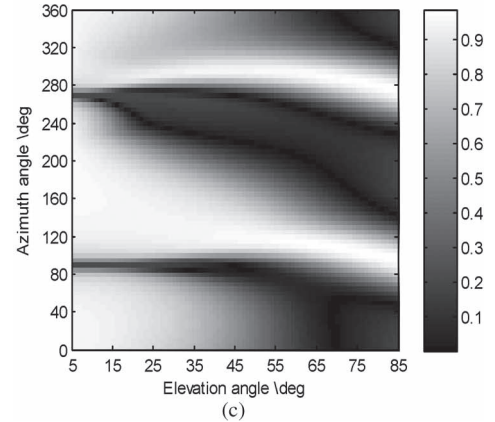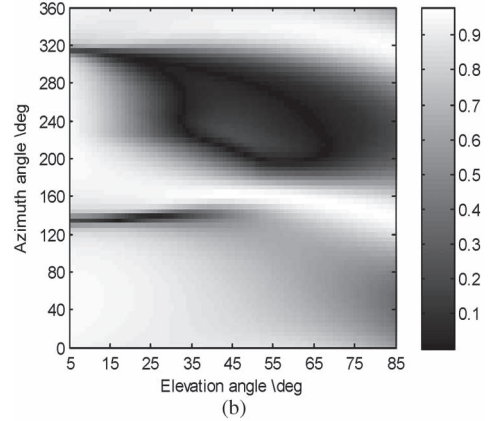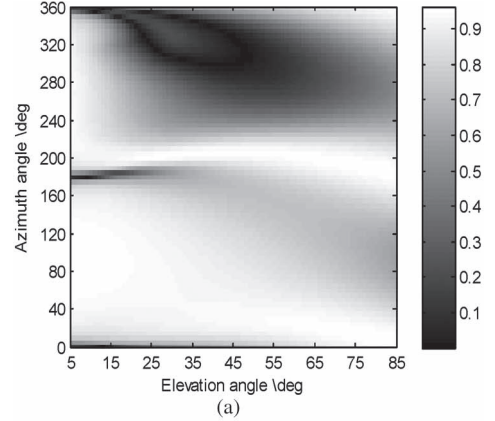
Fig. 7. Spatial decorrelation in the general bistatic configuration versus satellite azimuth/elevation angles for (a) v_1, parallel to the X-axis; (b) v_2, at a $45°$ angle to the X-/Y-axes; and (c) v_3, parallel to the Y-axis.

Without loss of generality, it is assumed that the position of the receiver is at $\alpha_R = 90°$ and $\beta_R = 5°$, while the position of a GLONASS satellite (α_T, β_T) varies (Fig. 6). The objective is to investigate the behavior of the spatial decorrelation with the different satellite positions for fixed azimuth and elevation offsets. Apart from the position of the satellite, its motion direction was also varied. That is because, from (4), it can be seen that the impulse response of the system is related to the effective angular velocity ω_E and Ξ of the satellite. For illustrative purposes, three representative motion directions are considered (Fig. 6): parallel to the X-axis, parallel to the Y-axis, and at a $45°$ angle to the X-/Y-axes.
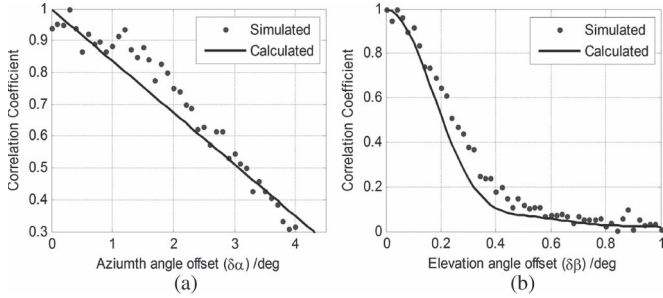
Fig. 8. Simulation result of the spatial decorrelation effect in the quasi-monostatic configuration. (a) Spatial decorrelation due to the azimuth angle's offset. (b) Spatial decorrelation due to the elevation angle's offset.

Fig. 9. Simulation result of the spatial decorrelation effect in the nadir-looking configuration.

Fig. 10. GNSS-based SAR experimental prototype.

The spatial decorrelation was numerically calculated using (13) for the different conditions mentioned previously. In the calculations, the satellite azimuth angle is chosen as $0° \leq \alpha_T < 360°$, and its elevation angle is $5° \leq \beta_T \leq 85°$. The obtained results are plotted in Fig. 7 for equal azimuth and elevation offsets of $\Delta\alpha = \Delta\beta = 0.1°$, which can be expected in practice.

Fig. 7 demonstrates the dependence of the spatial decorrelation on the data acquisition geometry. For the same angular offsets, spatial decorrelation varies with the satellite position as well as its motion direction. In addition, the figure shows that some bistatic configurations are more immune to spatial decorrelation than others. For example, in Fig. 7(a), for $\alpha_T = 50°$ and $\beta_T = 70°$, the correlation coefficient is higher than 0.9, whereas for $\alpha_T = 275°$ and $\beta_T = 70°$, it is lower than 0.3 for the same angular offset. This means that CCD schemes should be built around the particular data acquisition geometries to minimize spatial errors.

IV. SIMULATION

In this section, the validity of the analytical derivations made previously is tested using Monte Carlo simulations. It is assumed that a set of 10 000 scattering centers is located randomly within a resolution cell. Based on (2) and (4), the corresponding image signal s_1 was obtained by coherent superposition. Subsequently, changes in the satellite's position were added, and the corresponding image signal s_2 was calculated in the same way. The correlation coefficient between the two images was then calculated directly using (1). This process was repeated 1000 times to get the ensemble average. This number of realizations was established by trial and error, and beyond this number, the difference in obtained results was insignificant.

A comparison between the simulated and theoretical results for the quasi-monostatic configuration is shown in Fig. 8. It can be seen that the simulation result is in agreement with the theoretical derivation. Any difference between the simulated and theoretical results is accredited to the truncated impulse response used in the simulations. This is not a special problem in BSAR and has also been encountered with monostatic SAR data [21].

Similarly, Fig. 9 compares the theoretical and simulated results for the nadir-looking configuration. In this case, there is almost a one-to-one correspondence between the obtained results.

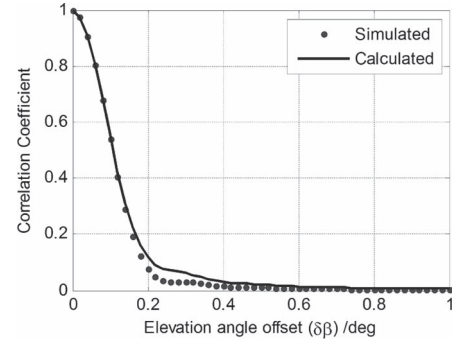Comparison of analytical results with simulated ones supports the validity of the developed theoretical models for the quasi-monostatic and nadir-looking configurations. This also implies that the "speckle" model offers a reasonable description of the GNSS-based SAR image signal, and this theory applies also for the more general BSAR case with a spaceborne transmitter and a fixed receiver. Furthermore, from the decorrelation values obtained, it can be seen that the corresponding configurations can be realized in practice to deliver a CCD based on GNSS-based SAR.
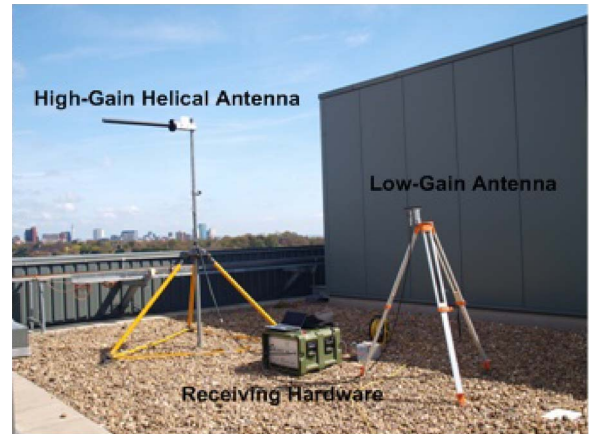
To confirm the theoretical model for the general bistatic configuration, working with experimentally obtained data was preferred to simulated ones. The experimental methodology and results, as well as their comparison with the developed theoretical model, are presented in the next section.

V. EXPERIMENTAL VERIFICATION

Experiments were conducted to measure spatial image decorrelation using experimental GNSS-based SAR data and to compare it to the theoretical expectations based on the aforementioned analysis. The geometrical configuration of the experimental data belongs to the general bistatic configuration. Data were acquired by a prototype system, developed at the University of Birmingham [6] and deployed on the roof of a five-story building (Fig. 10). The system used a low-gain antenna pointed toward the satellite for signal synchronization, while a high-gain helical antenna was pointed toward an observation area for imaging. The details of the imaging experiment conducted are listed in Table II.

TABLE II
EXPERIMENTAL PARAMETERS

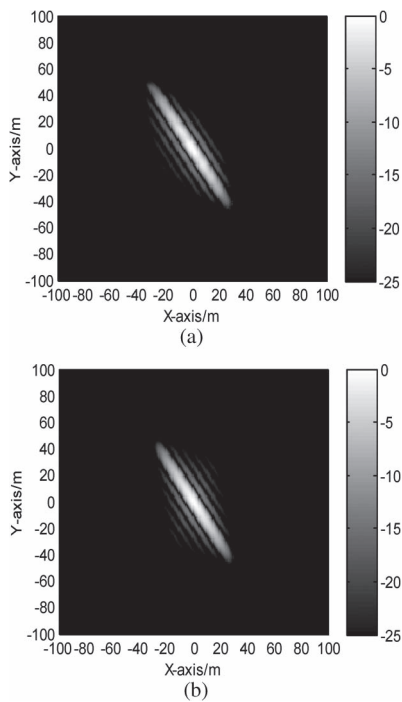| Parameters	Value
Satellite effective velocity	3395 m/s
Carrier Frequency	1604.8125 MHz
Signal Bandwidth	5.11 MHz
Integration Time	250 s
Satellite-to-Target Range r_{T0}	19516 Km
Transmitter Azimuth Angle	157.4 deg
Transmitter Elevation Angle	67.8 deg
Receiver Azimuth Angle	180 deg
Receiver Height	35 m

Fig. 11. (a) Experimentally obtained PSF. (b) Theoretical expectation.

As a first test on the experimental data and the image formation outputs, image formation was applied to the direct satellite signal recorded through the low-gain antenna. Effectively, this signal served as a point target located at zero range from the receiver. Therefore, the output of the image formation algorithm in this case should be the corresponding PSF. This PSF was then compared to the theoretically expected one from the relative satellite-receiver geometry [17]. The two results are shown in Fig. 11. The color scale in the figure is in decibels, with 0 dB representing the highest intensity in the image.

Comparison of the PSFs in Fig. 11 shows a nearly one-to-one correspondence between the experimental and theoretical results, verifying the validity of the experimental data. As a next step, image formation was applied to signals reflected from the observation area to obtain its image, using all of the available dwell time on target (250 s). Fig. 12(a) shows a satellite photograph of the area, obtained from Google Earth. Fig. 12(b) shows the obtained image, superimposed on the
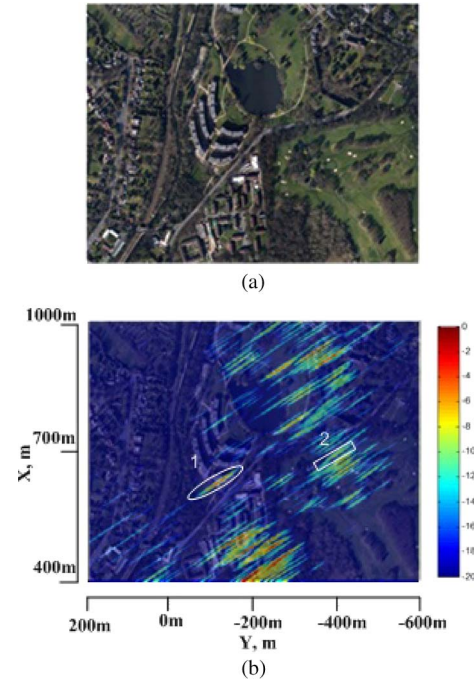

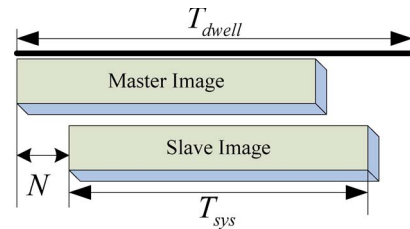Fig. 12. (a) Satellite photograph of the observation area. (b) GNSS-based SAR image superimposed on (a).

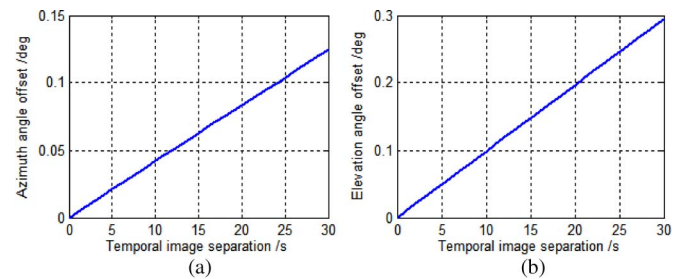Fig. 13. Master and slave images scheme for spatial decorrelation measurement.

Fig. 14. Satellite (a) azimuth and (b) elevation angle offsets versus the temporal separation between images.

photograph of Fig. 12(a). The color scheme in the figure is the same as in Fig. 11.

Inspection of Fig. 12 shows that the image echo intensity matches well with the expected reflectivity of the scene. For example, buildings (area 1) and trees (area 2) appear as high-intensity echoes, while grassy areas have low intensity values.

To evaluate spatial decorrelation, as well as its variation with the difference in satellite viewing angles, the following methodology was followed. A master image was generated, using data from the start time of acquisition and for a dwell time T_{sys} that was less than the dwell time on target (Fig. 13).
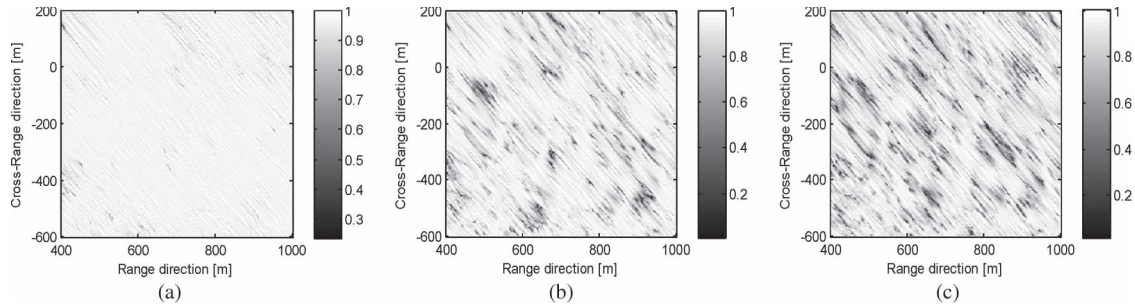
Fig. 15.   Coherence maps for (a) 1-, (b) 10-, and (c) 20-s temporal separation between the master and slave images.

Then, a set of slave images was generated, with the same $T_{\rm sys}$ but starting N seconds later than the master image, with N from 1 to 30 s. In other words, N is the temporal separation between images. It is noted here that all images were formed on exactly the same ground plane using a backprojection algorithm, and therefore, an image coregistration step was not required. The different temporal separations correspond to different satellite viewing angles in each image, allowing spatial decorrelation to be measured by extracting the correlation coefficients between the master image and all of the slave images through (1). This methodology was chosen for three main reasons. First of all, since all images were obtained from the same data set, thermal and temporal decorrelation should be minimal, allowing the measurement of only spatial decorrelation. Second, varying the temporal separation between images could allow a visualization of how spatial decorrelation varies with the satellite viewing angles. As listed in Table II, the reference azimuth and elevation angles are 157.4° and 67.8°, respectively. The variation of the satellite azimuth and elevation angle offsets with respect to the time offset is shown in Fig. 14. It can be seen that, even with 30-s separation, which is not realistic from practical experience (repeat-pass satellite measurements have been made with a minimum of 1-s accuracy [18]), the difference between satellite viewing angles is only fractions of a degree. This is because navigation satellites are in medium Earth orbit, allowing for very long distances to any point on Earth. Finally, this scheme simulates a real repeat-pass acquisition, where the repeat-pass image is acquired with some time offset due to practical reasons.

Example coherence maps between the master image and slave images with temporal separations of 1, 10, and 20 s are shown in Fig. 15. These maps show the correlation coefficient between images, computed using a spatial sliding window, 20 by 20 points wide, in a similar fashion to [25].

As expected, Fig. 15 shows that, as the temporal separation (and therefore angular separation) between images increases, the coherence between them decreases.

To compare experimental spatial decorrelation results with theoretical ones, as shown in Fig. 12(b), two representative areas within the image were selected. The first one is located around $(630, -116)$ m in the image of Fig. 12. In this area, there is a strong compressed echo from a single building, which is a student accommodation hall [Fig. 16(a)]. The second one is located around $(694, -398)$ m and contains a patch of trees [Fig. 16(b)], which were also detected with a sufficiently high signal-to-noise ratio (SNR).

Fig. 16.   Objects selected for spatial decorrelation evaluation within the imaging scene. (a) Building. (b) Trees.

For both targets, the SNR and the signal-to-background ratio (SBR) [29] were estimated. The first parameter is the ratio between the compressed echo intensity for the targets in question and the mean receiver thermal noise level, while the second parameter is the ratio between the compressed echo intensity for the same targets and the mean echo intensity of areas in the image where there are no distinct objects (e.g., flat grassy areas), which we define as "background." The background consists of receiver thermal noise, compressed echo sidelobes from other targets in the image (since the transmitted waveform is a pseudorandom sequence, transmitted continuously), and terrain reflections. The mean thermal noise level was found by measuring the noise floor of our receiver, while the mean background level was estimated directly from the obtained image in Fig. 12. The SNR/SBR values for the building and tree areas were found to be 22.41/21.9 and 17.27/16.7 dB, respectively, which were sufficient for further processing. It is also noted here that both target areas were located at distances between 650 and 700 m from the receiver, while at the application level, it is expected that the receiver would be placed no more than 200 m than the area to be monitored. It is also worth mentioning that, according to these figures, an intensity level of -20 dB in the image of Fig. 12 is dominated by receiver thermal noise.

The coherence between the master and slave images for different time offsets was recorded from the obtained coherence maps for each of the objects in Fig. 16. The reader is prompted to Fig. 14 to translate time offsets to the particular satellite azimuth/elevation angle. The measured coherence plots are shown in Fig. 17. For comparison, the corresponding theoretical coherence values were calculated based on (13) and the experimental parameters and were plotted on the same graph. Averaging windows, 20×20 pixels (image samples) wide, were used for the evaluation of the experimental curves in Fig. 17.
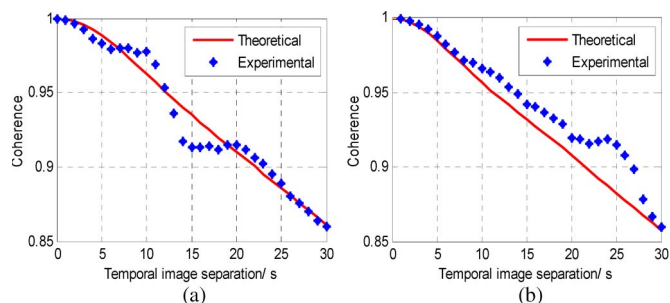
Fig. 17. Experimental versus theoretically predicted spatial coherence for (a) building area and (b) tree area.

Fig. 17 shows that the experimentally obtained spatial coherence is consistent with the theoretical predictions made using the model developed in this paper, confirming its validity. It also shows that, in GNSS-based SAR, spatial decorrelation effects are not so dramatic as in the traditional spaceborne SAR cases and can be further minimized by choosing the appropriate satellite trajectories for change detection. In this example, even a time offset of 15 s between repeat passes leads to a spatial coherence higher than 0.9. There are some deviations between the theoretical and practical results in Fig. 17, which may be attributed to the complexity of the target structures and the experiment itself. Even so, these deviations appear at temporal image separations (10 s or longer) which are not expected in practice.

VI. CONCLUSION

This paper has described spatial decorrelation and its effects in CCD using GNSS-based SAR. A theoretical model has been developed for this case by extending existing monostatic SAR theory, and it was verified using both simulated and experimental data. This model can also be applied to the generic BSAR case. It was found that spatial coherence is sensitive to the data acquisition geometries to a high degree, where, in many cases, a complete loss of coherence can occur for very small geometrical errors. However, there were many cases where the data collection geometry is much more robust to such errors, and these are the recommended geometries for the further CCD exploitation. Having already found in previous work that our system is robust to atmospheric errors too, the next step in this research is to conduct full-scale trials to assess the practical performance of GNSS-based SAR for CCD.

REFERENCES

[1] I. Walterscheid, J. H. G. Ender, A. R. Brenner, and O. Loffeld, "Bistatic SAR processing and experiments," *IEEE Trans Geosci. Remote Sens.*, vol. 44, no. 10, pp. 2710–2717, Oct. 2006.

[2] M. Rodriguez-Cassola, S. V. Baumgartner, G. Krieger, and A. Moreira, "Bistatic TerraSAR-X/F-SAR spaceborne-airborne SAR experiment: Description, data processing, results," *IEEE Trans Geosci. Remote Sens.*, vol. 48, no. 2, pp. 781–794, Feb. 2010.

[3] I. Walterscheid *et al.*, "Bistatic experiments with PAMIR and TerraSAR-X-setup, processing, and image results," *IEEE Trans Geosci. Remote Sens.*, vol. 48, no. 8, pp. 3268–3279, Aug. 2010.

[4] J. Sanz-Marcos, P. Lopez-Dekker, J. J. Mallorqui, A. Aguasca, and P. Prats, "SABRINA: A SAR bistatic receiver for interferometric application," *IEEE Geosci. Remote Sens. Lett.*, vol. 4, no. 2, pp. 307–311, Apr. 2007.

[5] A. S. Goh, M. Preiss, N. J. S. Stacy, and D. A. Gray, "Bistatic SAR experiment with the Ingara imaging radar," *IET Radar Sonar Navigat.*, vol. 4, no. 3, pp. 426–437, Jun. 2010.

[6] G. Krieger *et al.*, "TanDEM-X: A satellite formation for high-resolution SAR interferometry," *IEEE Trans Geosci. Remote Sens.*, vol. 45, no. 11, pp. 3317–3341, Nov. 2007.

[7] S. Duque. P. Lopez-Dekker, J. J. Mallorqui, and J. C. Merlano, "Repeat-pass interferometry using a fixed-receiver and ERS-2/ENVIST as transmitters of opportunity," in *Proc. IEEE Int. Geosci. Remote Sens. Symp.*, Jul. 2009, pp. 246–249.

[8] S. Duque. P. Lopez-Dekker and J. J. Mallorqui, "Single-pass bistatic SAR interferometry using fixed-receiver configurations: Theory and experimental validation," *IEEE Trans Geosci. Remote Sens.*, vol. 48, no. 6, pp. 2740–3749, Jun. 2010.

[9] Y. Shao *et al.*, "Error analysis of bistatic SAR imaging and stereoscopy bistatic SAR," *IEEE Trans Geosci. Remote Sens.*, vol. 51, no. 8, pp. 4518–4543, Aug. 2013.

[10] M. Cherniakov, Ed., *Bistatic Radar: Emerging Technology*. Hoboken, NJ, USA: Wiley, 2008.

[11] M. Cherniakov, R. Saini, R. Zuo, and M. Antoniou, "Space-surface bistatic synthetic aperture radar with Global Navigation Satellite System transmitter of opportunity—Experimental results," *IET Radar Sonar Navigat.*, vol. 1, no. 6, pp. 447–458, Dec. 2007.

[12] M. Antoniou, R. Saini, and M. Cherniakov, "Results of a space-surface bistatic SAR imaging formation algorithm," *IEEE Trans Geosci. Remote Sens.*, vol. 45, no. 11, pp. 3359–3371, Nov. 2007.

[13] M. Antoniou, M. Cherniakov, and C. Hu, "Space-surface bistatic SAR imaging formation algorithm," *IEEE Trans Geosci. Remote Sens.*, vol. 47, no. 6, pp. 1827–1843, Jun. 2009.

[14] M. Antoniou and M. Cherniakov, "GNSS-based bistatic SAR: A signal processing view," *EURASIP J. Adv. Signal Process.*, vol. 2013, no. 1, pp. 1–16, 2013.

[15] M. Cherniakov, E. Plakids, M. Antoniou, and R. Zuo, "Passive space-surface bistatic SAR for local area monitoring: Primary feasibility study," in *Proc. EuRad*, 2009, pp. 89–92.

[16] M. Antoniou, Z. Zeng, F. Liu, and M. Cherniakov, "Experimental demonstration of passive BSAR imaging using navigation satellites and a fixed receiver," *IEEE Geosci. Remote Sens. Lett.*, vol. 9, no. 3, pp. 477–481, May 2012.

[17] F. Liu, M. Antoniou, Z. Zeng, and M. Cherniakov, "Point spread function analysis for BSAR with GNSS transmitters and long dwell times: Theory and experimental confirmation," *IEEE Geosci. Remote Sens. Lett.*, vol. 10, no. 4, pp. 781–785, Jul. 2013.

[18] F. Liu, M. Antoniou, Z. Zeng, and M. Cherniakov, "Coherent change detection using passive GNSS-based BSAR: Experimental proof of concept," *IEEE Trans Geosci. Remote Sens.*, vol. 51, no. 8, pp. 4544–4555, Aug. 2013.

[19] M. Preiss and N. J. S. Stacy, "Coherent change detection: Theoretical description and experimental results," Defence Science and Technology Organisation, Canberra, ACT, Australia, DSTO-TR-1851, 2006.

[20] R. Bamler and P. Hartl, "Synthetic aperture radar interferometry," *Inverse Problem*, vol. 14, no. 4, pp. 9–27, 1998.

[21] H. A. Zebker and J. Villasenor, "Decorrelation in interferometric radar echoes," *IEEE Trans Geosci. Remote Sens.*, vol. 30, no. 5, pp. 950–959, Sep. 1992.

[22] E. Rodriguez and J. M. Martin, "Theory and design of interferometric synthetic aperture radars," *IEE Proc.-F*, vol. 139, no. 2, pp. 147–159, Apr. 1992.

[23] F. K. Li and R. M. Goldstein, "Studies of multi-baseline spaceborne interferometric synthetic aperture radars," *IEEE Trans Geosci. Remote Sens.*, vol. 28, no. 1, pp. 88–97, Jan. 1990.

[24] F. Gatelli *et al.*, "The wavenumber shift in SAR interferometry," *IEEE Trans Geosci. Remote Sens.*, vol. 32, no. 4, pp. 855–865, Jul. 1994.

[25] C. Prati and F. Rocca, "Improving slant range resolution of stationary objects with multiple SAR surveys," *IEEE Trans. Aerosp. Electron. Syst.*, vol. 29, no. 1, pp. 135–144, Jan. 1993.

[26] T. Wang, Z. Bao, Z. Zhang, and J. Ding, "Improving coherence of complex image pairs obtained by along-track bistatic SARs using range-azimuth prefiltering," *IEEE Trans Geosci. Remote Sens.*, vol. 46, no. 1, pp. 3–13, Jan. 2008.

[27] J. M. Goodman, "Statistical properties of laser speckle patterns," *Topics Appl. Phys.*, vol. 9, pp. 9–75, 1975.

[28] T. Zeng, M. Cherniakov, and T. Long, "Generalized approach to resolution analysis in BSAR," *IEEE Trans. Aerosp. Electron. Syst.*, vol. 41, no. 2, pp. 461–474, Apr. 2005.

[29] M. Antonio *et al.*, "Passive bistatic synthetic aperture radar imaging with Galileo transmitters and a moving receiver: Experimental demonstration," *IET Radar Sonar Navigat.*, vol. 7, no. 9, pp. 985–993, Dec. 2013.

Qilei Zhang received the B.S. degree in communication engineering and the M.S. degree in information and communication engineering from the National University of Defense Technology, Changsha, China, in 2007 and 2009, respectively, where he is currently working toward the Ph.D. degree.

From January 2012 to July 2013, he was a visiting Ph.D. student with the University of Birmingham, Birmingham, U.K. His fields of interest include bistatic synthetic aperture radar synchronization, imaging, and interferometric applications.

Wenge Chang received the B.S. and Ph.D. degrees from the National University of Defense Technology, Changsha, China, in 1987 and 2001, respectively.

From December 2007 to June 2008, he was an academic visitor with the University of Birmingham, Birmingham, U.K. He is currently a Professor with the National University of Defense Technology. His fields of interest include synthetic aperture radar and array signal processing.

Michail Antoniou, photograph and biography not available at the time of publication.

Mikhail Cherniakov, photograph and biography not available at the time of publication.